

Frustration driven magnetic correlations in the spin-5/2 triangular lattice antiferromagnet $\text{RbFe}(\text{HPO}_3)_2$

V. Nagpal,¹ Sebin J. Sebastian,^{1,2} Surya P. Patra,¹ S. Shibash,¹ Q.-P. Ding,² Y. Furukawa,^{2,3} and R. Nath^{1,*}

¹*School of Physics, Indian Institute of Science Education and Research Thiruvananthapuram-695551, India*

²*Ames National Laboratory, U.S. DOE, Iowa State University, Ames, Iowa 50011, USA*

³*Department of Physics and Astronomy, Iowa State University, Ames, Iowa 50011, USA*

(Dated: November 24, 2025)

A detailed study of the structural and magnetic properties of a spin-5/2 triangular lattice antiferromagnet $\text{RbFe}(\text{HPO}_3)_2$ is presented using x-ray diffraction, magnetization, heat capacity, and ^{31}P nuclear magnetic resonance (NMR) experiments on a polycrystalline sample. The crystal structure features an equilateral triangular lattice of Fe^{3+} ions. The thermodynamic measurements reveal the onset of a magnetic long-range order at $T_{\text{N}1} \simeq 7.8$ K in zero-field, followed by another low temperature field induced ordering at $T_{\text{N}2}$ in higher fields. The transition at $T_{\text{N}1}$ is further confirmed from the NMR spin lattice relaxation measurements. The value of the frustration ratio ($f \simeq 7$) implies moderate spin frustration in the compound. The ^{31}P NMR spectra exhibit two distinct spectral lines corresponding to two inequivalent phosphorus sites (P1 and P2), consistent with the crystal structure. The P1 site is strongly coupled with an isotropic hyperfine coupling of $A_{\text{hf}}^{\text{iso}} = 0.55(2)$ T/ μB while the P2 site is weakly coupled with $A_{\text{hf}}^{\text{iso}} = 0.25(3)$ T/ μB with the Fe^{3+} ions. The magnetic susceptibility and NMR shift data are described well assuming a spin-5/2 isotropic triangular lattice antiferromagnetic model with an average exchange coupling of $J/k_{\text{B}} = 2.8(2)$ K. Below $T_{\text{N}1}$, the spectra evolve into a nearly rectangular powder pattern, indicating a commensurate antiferromagnetic type order. The ^{31}P spin-lattice relaxation rate well below $T_{\text{N}1}$ follows a T^3 temperature dependence, implying a two-magnon Raman scattering mechanism in the ordered state. Three well-defined phase regimes are clearly ascertained in the $H-T$ phase diagram, reflecting a weak magnetic anisotropy in the compound.

I. INTRODUCTION

The triangular-lattice antiferromagnet (TLAF) has long been regarded as a cornerstone in the study of frustrated magnetism [1]. The incompatibility of anti-ferromagnetic (AFM) exchange interactions on a triangular geometry suppresses conventional Néel order and produces a highly degenerate manifold of states. This intrinsic degeneracy makes TLAFs exceptionally sensitive to fluctuations. However, the quantum and thermal fluctuations lift this degeneracy through an order-by-disorder mechanism, resulting in unconventional magnetic ground states. One of the most celebrated possibilities is the quantum spin liquid (QSL), a highly entangled state without magnetic long-range order (LRO), first envisioned by Anderson in the form of a resonating-valence-bond state for spin-1/2 TLAFs [2, 3]. Later, both theoretical and experimental studies established that the ideal isotropic TLAF instead stabilizes in a chiral three-sublattice 120° spin configuration, for any spin value [4, 5]. Importantly, this canonical state is not immutable: perturbations such as exchange anisotropy, interlayer coupling, and external magnetic field can destabilize the 120° order and yield a variety of exotic phases in both quantum ($S = 1/2$) and classical ($S > 1/2$) limits [6–9].

These theoretical considerations are vividly realized in a broad range of materials. Prototypical examples in-

clude ABX_3 halides ($A = \text{Cs, Rb}; B = \text{V, Mn, Ni}; X = \text{Cl, Br, I}$) [10, 11] and $\text{Ba}_3\text{MZ}_2\text{O}_9$ ($M = \text{Mn, Co, Ni}; Z = \text{Sb, Nb, Ta}$) [12–14], along with other compounds hosting triangular layers [15–18]. More recently, members of the *yavapaiite* family $AM(\text{XO}_4)_2$ ($A = \text{K, Rb, Cs, Ba}; M = \text{Fe, Ti, Mo}; X = \text{S, Mo, P}$) have emerged as exemplary quasi-2D TLAFs displaying unusual quantum phases and complex field-dependent properties [6, 19–25]. Within this family, the degree of lattice symmetry crucially determines the ground state. For instance, equilateral TLAFs such as $A\text{Fe}(\text{SO}_4)_2$ ($A = \text{Rb, Cs}$) and $A\text{Fe}(\text{MoO}_4)_2$ ($A = \text{K, Rb, Cs}$) stabilize three-sublattice 120° order in the basal plane [19, 20, 22, 23, 26], whereas monoclinic compounds including $KT(\text{SO}_4)_2$ ($T = \text{Fe, Ti}$) and $\text{BaMo}(\text{PO}_4)_2$ favor isosceles triangular motifs with collinear AFM order [21, 25].

An intriguing extension is provided by the *oxofluorophosphate* family $A\text{Fe}(\text{PO}_3\text{F})_2$ [$A = \text{K, (NH}_4\text{)}_2\text{Cl, NH}_4, \text{Rb, Cs}$], in which the $\text{Fe}(\text{PO}_3\text{F})_2$ layers are structurally identical to $M(\text{XO}_4)_2$ layers of the *yavapaiite* family [27]. While all the members order antiferromagnetically, their ground states and field responses are diverse. For example, trigonal $K\text{Fe}(\text{PO}_3\text{F})_2$ hosts a coplanar 120° order coexisting with commensurate non-centrosymmetric stacking along the c axis, whereas $\text{NH}_4\text{Fe}(\text{PO}_3\text{F})_2$ exhibits a weak XY anisotropy manifested as a field-induced spin-flop transition [28]. These discoveries highlight the richness of the *yavapaiite* and *oxofluorophosphate* based TLAFs, pondering the fact that subtle perturbations may destabilize the canonical 120° state and give rise to unconventional field-induced

* rameshchandra.nath@gmail.com

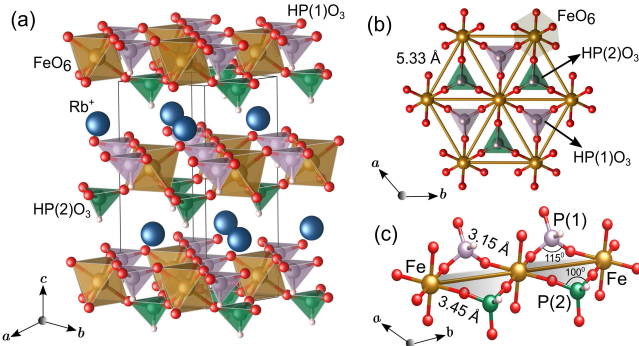


FIG. 1. (a) Crystal structure of $\text{RbFe}(\text{HPO}_3)_2$ showing triangular layers of Fe atoms formed by the corner-shared FeO_6 octahedra and HPO_3 pseudo-tetrahedra. Rb^+ ions separate the two adjacent triangular layers. (b) A section of the layer showing Fe^{3+} ions connected through HPO_3 pseudo-tetrahedra in a triangular lattice. (c) Schematic picture showing different environments for $\text{P}(1)$ and $\text{P}(2)$ sites with respect to Fe atoms.

phases.

In this work, we present a detailed study of the spin-5/2 frustrated *yavapaiite*-type phosphate compound $\text{RbFe}(\text{HPO}_3)_2$ (RFHPO) by means of dc and ac magnetic, thermodynamic, and nuclear magnetic resonance (NMR) measurements. RFHPO belongs to the family of compounds $A^{1+}M^{3+}(\text{HPO}_3)_2$ [$A = \text{K, NH}_4, \text{Rb}$ and $M = \text{V, Fe}$] and crystallizes in a hexagonal structure with space group $P6_3mc$ (No. 186) at room temperature [29]. The crystal structure of RFHPO is presented in Fig. 1(a) in which Fe^{3+} ions form an FeO_6 octahedra and corner-share with pseudo-tetrahedra phosphate group HPO_3 in order to form the triangular Fe^{3+} layers in the ab -plane. These planes are stacked parallel to each other along the c -axis, separated by the non-magnetic Rb^+ ions. The Fe^{3+} ions from the adjacent layers are connected via weak hydrogen bonds formed by the Fe-O-H-O-Fe pathway, which leads to negligible interlayer coupling. Further, it is found that Fe^{3+} - Fe^{3+} bond lengths in each triangular unit are equal, making equilateral triangles as shown in Fig. 1(b). No detailed magnetic measurements on RFHPO are available till date, apart from an earlier report that identified an AFM transition at around $T_N \simeq 9$ K from the bulk susceptibility data [29]. However, the microscopic nature of the ordered state and its field evolution remained unexplored. Our magnetic measurements reveal that RFHPO is a frustrated spin-5/2 TLAF that undergoes a magnetic LRO at $T_{\text{N}1} \simeq 7.8$ K despite a large negative Curie-Weiss temperature ($\theta_{\text{CW}} \simeq -52$ K), which is of commensurate AFM type. The H - T phase diagram divulges two magnetic phases, reflecting spin reorientation driven by a weak magnetic anisotropy and/or frustration.

II. METHODS

A polycrystalline sample of RFHPO was synthesized using the hydrothermal reaction method. The initial precursors 0.913 g Rb_2CO_3 (Aldrich, 99.9%), 0.534 g $\text{FeCl}_3 \cdot 6\text{H}_2\text{O}$ (Loba Chemie, 97%), and 0.608 g H_3PO_3 (Alfa Aesar, 99.8%) were taken and mixed in a 10 mL deionized water. The obtained mixture was immediately placed in a 23 mL Teflon-lined stainless steel autoclave and then heated to 180° C in an oven for 3 days followed by a slow cooling in 3 days. The resultant product was then washed with water/ethanol several times in order to remove any unwanted impurities and dried overnight at 100° C. Finally, a white-purplish coloured polycrystalline sample was obtained. Powder x-ray diffraction (XRD) of the resultant product was carried out at room temperature to confirm the phase purity using a PANalytical x-ray diffractometer (CuK_α radiation, $\lambda_{\text{avg}} \simeq 1.5418$ Å). Figure 2 shows the powder XRD pattern of RFHPO along with the Rietveld fit. All the diffracted peaks could be indexed with the hexagonal unit cell [$P6_3mc$], confirming single phase of the polycrystalline product. The obtained lattice parameters at room temperature after the refinement are $a = b = 5.33(1)$ Å, $c = 12.68(3)$ Å, and unit-cell volume $V_{\text{cell}} = 313.62(2)$ Å³, consistent with the previous report [29].

The dc magnetization (M) was measured as a function of temperature (2 K $\leq T \leq 380$ K) and magnetic field (0 $\leq \mu_0 H \leq 9$ T) using the VSM option of a Physical Property Measurement System (PPMS, Quantum Design). The ac magnetization was measured in the temperature range (2 K $\leq T \leq 30$ K) using the ACMS option of PPMS. The ac-measurements were done by varying the frequency (100 Hz $\leq f \leq 10$ KHz) in an applied ac field of $H_{\text{ac}} = 5$ Oe and then by varying the dc magnetic field (0.01 $\leq H_{\text{dc}} \leq 9$ T) keeping $H_{\text{ac}} = 5$ Oe and $f = 499$ Hz fixed. Similarly, heat capacity (C_p) as a function of T (2 K $\leq T \leq 200$ K) and H (0 $\leq \mu_0 H \leq 9$ T) was measured on a small piece of sintered pellet using the standard relaxation technique in PPMS.

Nuclear magnetic resonance (NMR) measurements were performed using a laboratory-built phase-coherent spin-echo pulse spectrometer over a temperature range 1.6 K $\leq T \leq 300$ K on the ^{31}P nucleus ($I = 1/2$) with a gyromagnetic ratio of $\gamma_{\text{N}}/2\pi = 17.2356$ MHz/T. The NMR data were collected at two different radio frequencies, $\nu = 77.1$ and 120.6 MHz, which correspond to magnetic fields of $\mu_0 H = 4.47$ and 7 T, respectively. The NMR spectra were obtained by sweeping the magnetic field at a fixed resonance frequency, employing a standard $\pi/2 - \tau - \pi$ pulse sequence with $\tau = 20$ μs . The NMR shift $K(T)$ was extracted from the spectral peak position as $K = (2\pi\nu/\gamma_{\text{N}} - H_p)/H_p$, where H_p represents the magnetic field of the peak position at each temperature. The nuclear spin-lattice relaxation rate ($1/T_1$) was extracted by measuring the longitudinal magnetization as a function of waiting time by employing the saturation pulse sequence $\pi/2 - \tau_1 - \pi/2 - \tau_2 - \pi$, at the spectral

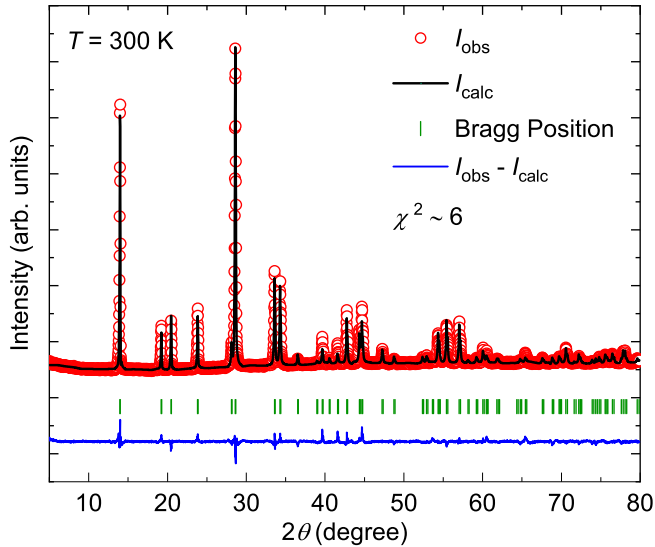


FIG. 2. Powder XRD data collected at room temperature. The red open circles are the experimental data, the black solid line is the Rietveld fit to the data, the vertical bars are the Bragg-peak positions, and the blue line at the bottom is the difference between the experimentally observed and calculated intensities.

TABLE I. Refined structural parameters of RFHPO obtained from the Rietveld refinement of the powder-XRD data collected at room temperature. Listed are the Wyckoff positions, refined atomic coordinates, and occupancy of each atom.

Atom	Wyckoff	<i>x</i>	<i>y</i>	<i>z</i>	Occ.
Rb1	2b	0.667	0.333	0.790(2)	1.000
Fe	2b	0.667	0.333	1.104(2)	1.000
P1	2b	0.333	0.667	0.967(1)	1.000
P2	2a	0	0	0.634(1)	1.000
O1	6c	0.520(1)	1.040(2)	0.978(2)	1.000
O2	6c	0.141(1)	0.282(2)	0.699(2)	1.000
H1	2b	0.333	0.667	0.783(2)	1.000
H2	2a	0	0	0.615(2)	1.000

peak positions.

Full diagonalization was performed using the `fulldiag` algorithm [30] of the ALPS package [31].

III. RESULTS AND DISCUSSION

A. Magnetization

Temperature-dependent dc magnetic susceptibility χ [$\equiv M/H$] measured in an applied magnetic field of $\mu_0 H = 0.5$ T is shown in the left y -axis of Fig. 3(a). In the high temperature region, $\chi(T)$ increases with lowering temperature following the Curie-Weiss (CW) behaviour. At low temperatures, it exhibits a broad peak

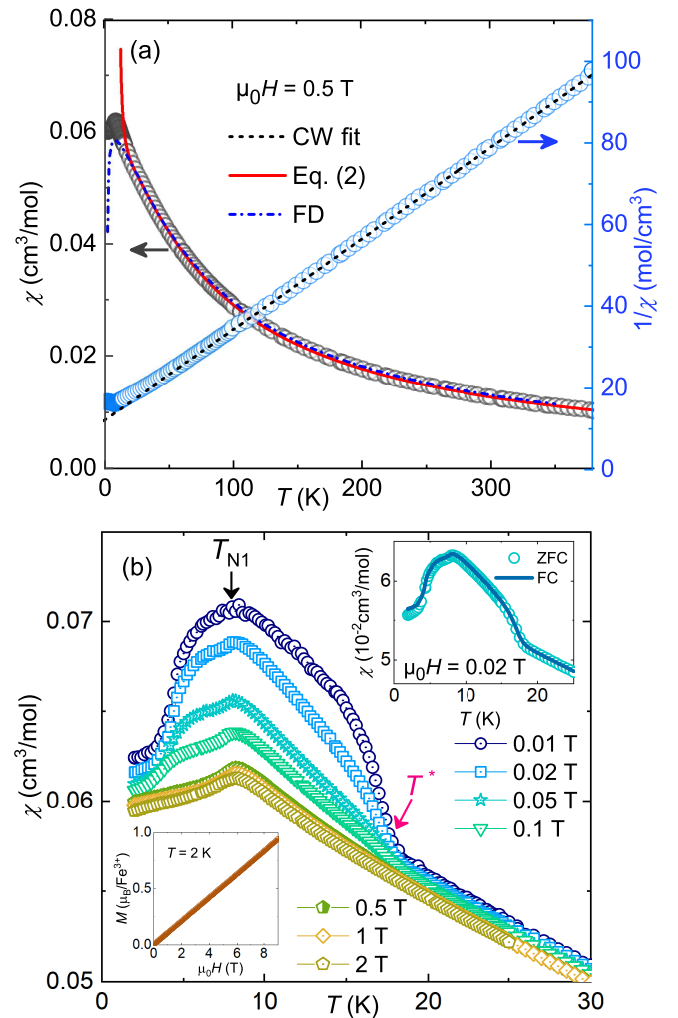


FIG. 3. (a) The dc magnetic susceptibility χ and its inverse $(1/\chi)$ as a function of temperature for $\mu_0 H = 0.5$ T in the left and right axes, respectively. The solid line represents the fit using the isotropic triangular lattice model to $\chi(T)$. The dash-dotted line is the simulation of $\chi(T)$ of a $S = 5/2$ isotropic TLAf using FD method. The dashed line represents the CW fit to $1/\chi(T)$. (b) χ vs T in various applied magnetic fields for $\mu_0 H \leq 2$ T. The arrows indicate the transitions at T_{N1} and T^* . Top inset: FC and ZFC $\chi(T)$ data measured at $\mu_0 H = 0.02$ T. Bottom inset: M vs H measured at $T = 2$ K.

at around $T_{N1} \simeq 8$ K, implying the transition to a magnetic LRO state. This transition temperature is slightly lower than the previous report [29]. To analyze the data, the inverse susceptibility $1/\chi$ for $T > 150$ K was fitted using the CW equation,

$$\chi(T) = \chi_0 + \frac{C}{(T - \theta_{CW})}. \quad (1)$$

Here, χ_0 is the temperature-independent susceptibility, C is the Curie constant, and θ_{CW} is the characteristic CW temperature. The fit yields $\chi_0 = -7.79(5) \times 10^{-5} \text{ cm}^3/\text{mol}$, $C = 4.50(4) \text{ cm}^3\text{K/mol}$, and $\theta_{CW} = -52.7(3)$ K. The large negative value of θ_{CW} indicates

dominant AFM interaction between Fe^{3+} ions. χ_0 comprises temperature-independent core diamagnetism and Van-Vleck paramagnetism. The core diamagnetic susceptibility (χ_{dia}) of RFHPO is calculated to be $-1.08 \times 10^{-4} \text{ cm}^3/\text{mol}$ by adding the core diamagnetic susceptibilities of elemental ions Rb^+ , Fe^{3+} , P^{5+} , O^{2-} , and H^+ [32]. The Van-Vleck paramagnetic susceptibility (χ_{vv}) is deduced to be $\sim 3 \times 10^{-5} \text{ cm}^3/\text{mol}$ by the subtraction of χ_{dia} from χ_0 . Using the value of C , the effective magnetic moment is calculated to be $\mu_{\text{eff}} = 6.0(1) \mu_B$ ($\mu_{\text{eff}} = \sqrt{3k_B C/N_A}$, where k_B is the Boltzmann constant, N_A is the Avogadro's number, and μ_B is the Bohr magneton). The obtained μ_{eff} is close to the expected spin-only effective moment for a spin-5/2 system with $g \simeq 2.03$.

While θ_{CW} represents the overall energy scale of the exchange interactions among the localized spins, the inherent geometrical frustration leads to the suppression of T_N as compared to θ_{CW} . Such a suppression of T_N is often used as an empirical measure of the magnetic frustration, quantified by the frustration index, $f (= |\theta_{\text{CW}}|/T_{N1})$. The value of f for RFHPO is calculated to be ~ 7 , indicating a moderate frustration. Similarly, the magnitude of θ_{CW} is defined as the sum of all possible exchange interactions $|\theta_{\text{CW}}| = JzS(S+1)/3k_B$, where z is the number of nearest neighbors of Fe^{3+} ions [33]. For RFHPO, taking $z = 6$ and $S = 5/2$, the average intralayer exchange coupling is calculated to be $J/k_B \simeq 3 \text{ K}$. In the Heisenberg TLA, the saturation field (H_{sat}) can be written in terms of J/k_B as $\mu_0 H_{\text{sat}} = 9JS/g\mu_B$ [16, 34]. In our case, with $J/k_B = 2.8 \text{ K}$ and $g = 2.03$, this value is calculated to be $\mu_0 H_{\text{sat}} \simeq 50 \text{ T}$.

Further, to model $\chi(T)$ and estimate the exchange coupling between the Fe^{3+} ions, $\chi(T)$ is divided into two components

$$\chi(T) = \chi_0 + \chi_{\text{spin}}(T). \quad (2)$$

Here, $\chi_{\text{spin}}(T)$ is the high temperature series expansion (HTSE) for a spin-5/2 Heisenberg isotropic TLA model given by [16, 35]

$$\frac{N_A \mu_B^2 g^2}{3|J|\chi_{\text{spin}}} = x + 4 + \frac{3.20}{x} - \frac{2.186}{x^2} + \frac{0.03}{x^3} + \frac{3.45}{x^4} - \frac{3.99}{x^5}, \quad (3)$$

where $x = k_B T / |J| S(S+1)$. This expression holds for $T \geq JS(S+1)$ [36]. As shown in Fig. 3(a), $\chi(T)$ above 30 K is fitted by Eq. (2) that yields $\chi_0 = -1.29(2) \times 10^{-4} \text{ cm}^3/\text{mol}$, $g = 2.01(1)$, and the average AFM exchange coupling $J/k_B = 2.8(2) \text{ K}$. Indeed, this value of J/k_B is in good agreement with the one obtained from θ_{CW} . To further establish the 2D TLA model, we also simulated $\chi(T)$ using full diagonalization method for a $S = 5/2$ TLA taking $J/k_B = 2.8 \text{ K}$. As seen in Fig. 3(a), it reproduces the overall shape of $\chi(T)$ data very well.

To assess the magnetic ground state of the system, we measured $\chi(T)$ at low fields ($\mu_0 H \leq 2 \text{ T}$), as shown in Fig. 3(b). At $\mu_0 H = 0.01 \text{ T}$, it features two distinct anomalies, labeled $T^* \simeq 17 \text{ K}$ and $T_{N1} \simeq 8.2 \text{ K}$. With increasing field, the broad hump at T^* is gradually reduced

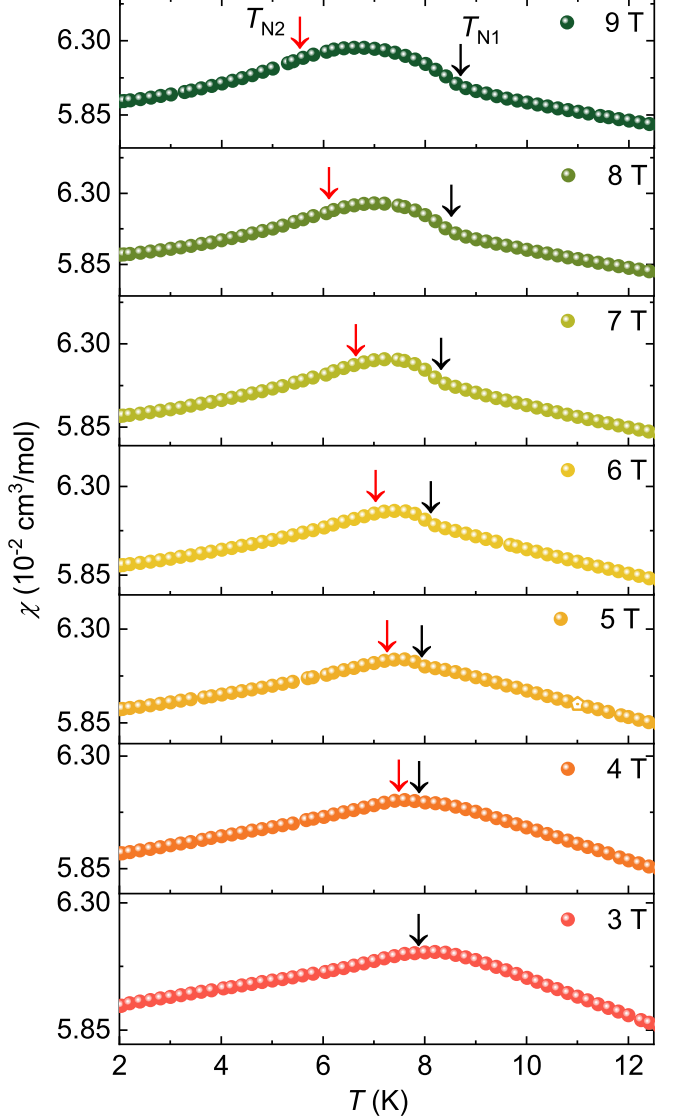


FIG. 4. Low temperature $\chi(T)$ in various applied fields $3 \text{ T} \leq \mu_0 H \leq 9 \text{ T}$. The vertical arrows indicate the two transitions, T_{N1} and T_{N2} , respectively.

and is completely suppressed for $\mu_0 H > 0.5 \text{ T}$. This feature possibly indicates the development of a weak FM correlation among the magnetic ions, which is a short-range type [37, 38]. Such a weak ferromagnetism could be arising due to a small spin canting triggered by magnetic anisotropy [39]. However, the anomaly at T_{N1} almost remains unchanged up to $\mu_0 H = 2 \text{ T}$. Further, we measured the field-cooled (FC) and zero-field-cooled (ZFC) $\chi(T)$ data at $\mu_0 H = 0.02 \text{ T}$ [top inset of Fig. 3(b)], which show no splitting at the transition temperatures, suggesting the absence of spin-freezing. The magnetization isotherm $M(H)$ measured at $T = 2 \text{ K}$ [bottom inset of Fig. 3(b)] shows an almost linear increase without reaching saturation up to 9 T, consistent with the dominant AFM exchange interaction in RFHPO.

Figure 4 presents $\chi(T)$ measured in different applied

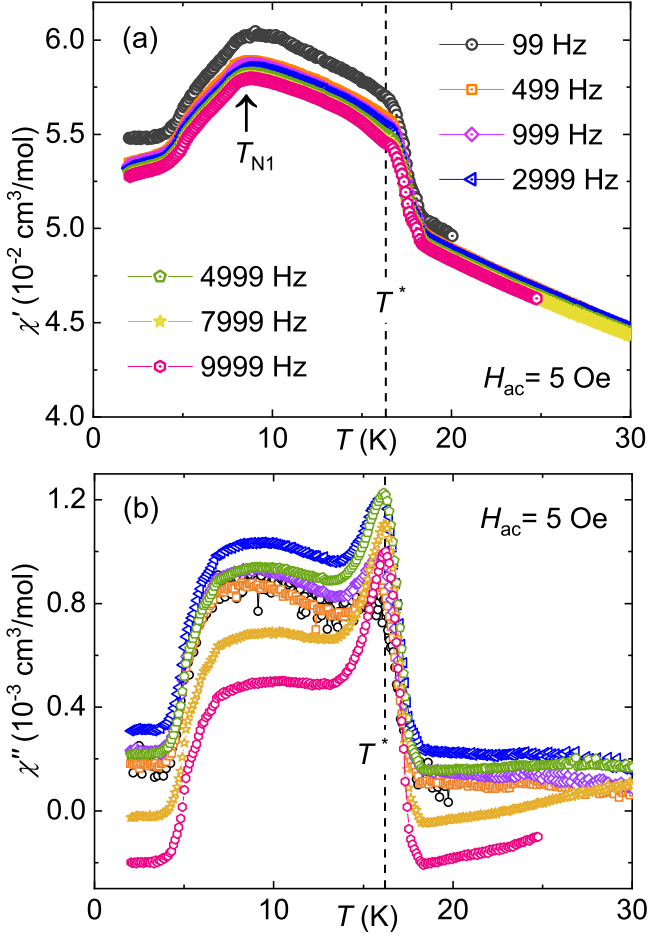


FIG. 5. (a) Temperature dependence of χ' measured in different frequencies. The transitions at T_{N1} and T^* are highlighted. (b) χ'' vs T measured in different frequencies.

magnetic fields, $3 \text{ T} \leq \mu_0 H \leq 9 \text{ T}$. For $\mu_0 H \leq 3 \text{ T}$, the anomaly at T_{N1} remains almost unchanged. However, for $\mu_0 H > 3 \text{ T}$, T_{N1} moves towards higher temperatures and another field induced kink (T_{N2}) appears which moves to lower temperature with increasing field. These two transitions are distinctly visible in the $d\chi/dT$ vs T plots (not shown). Such a field-induced transition has also been reported in other high-spin, low-dimensional TLAJs [26, 27, 40, 41]. These two transitions are further corroborated by our ac susceptibility and heat capacity measurements, discussed in the following sections.

B. AC susceptibility

To further investigate the magnetic transitions in zero dc field, we performed ac susceptibility measurements in an applied ac field of $H_{\text{ac}} = 5 \text{ Oe}$ at various frequencies. As shown in Fig. 5(a), the real part of ac susceptibility $\chi'(T)$ exhibits behavior similar to the low-field dc $\chi(T)$ data. It shows an asymmetric profile with a kink at $T_{N1} \approx 7.8 \text{ K}$. In addition, a hump appears near

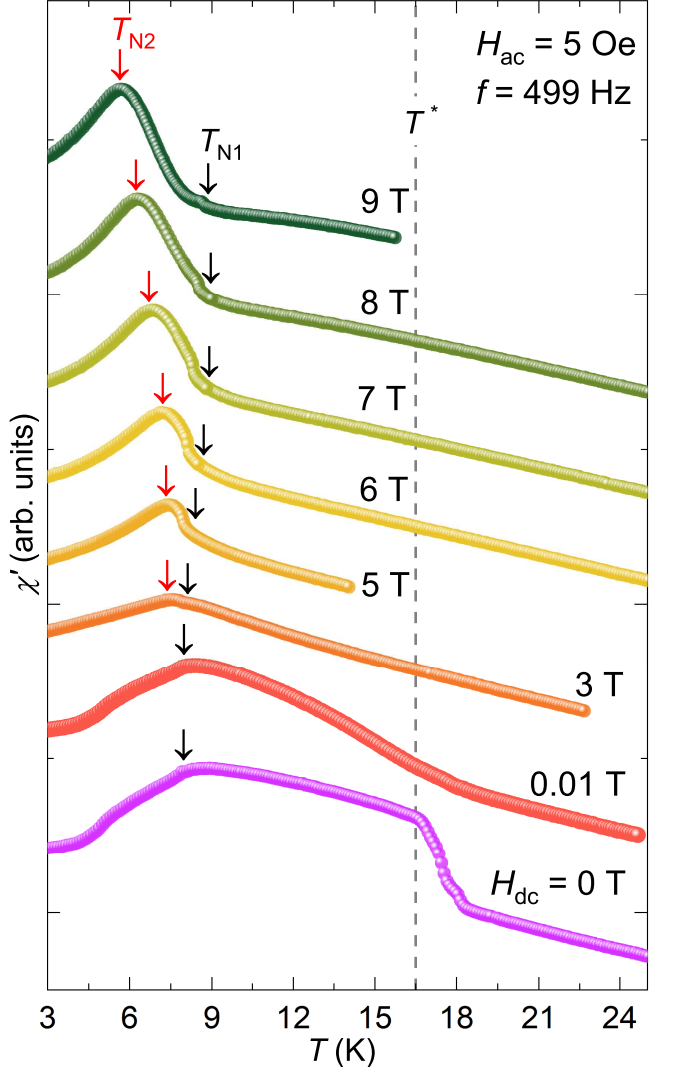


FIG. 6. χ' vs T at various applied dc fields and at a fixed frequency $f = 499 \text{ Hz}$. The data are vertically translated for clarity.

$T^* \approx 16 \text{ K}$, consistent with the anomaly observed in low field dc $\chi(T)$. The imaginary part $\chi''(T)$ [see Fig. 5(b)] also displays a sharp peak at T^* along with a broad shoulder near T_{N1} . Both the features in $\chi'(T)$ and $\chi''(T)$ are found to be frequency independent.

To probe the field-induced transition, we measured $\chi'(T)$ in different dc fields (see Fig. 6) at a fixed frequency $f = 499 \text{ Hz}$ and $H_{\text{ac}} = 5 \text{ Oe}$. In zero dc field, both T_{N1} and T^* are clearly visible. With increasing dc field, T^* is completely suppressed, confirming its origin as short-range FM correlation. For $H_{\text{dc}} \geq 3 \text{ T}$, $\chi'(T)$ shows a kink associated with T_{N1} followed by another peak at lower temperatures, corresponding to the second transition T_{N2} . With further increase in dc field, T_{N1} shifts to higher temperatures, while T_{N2} moves to lower temperatures, similar to the dc $\chi(T)$ data.

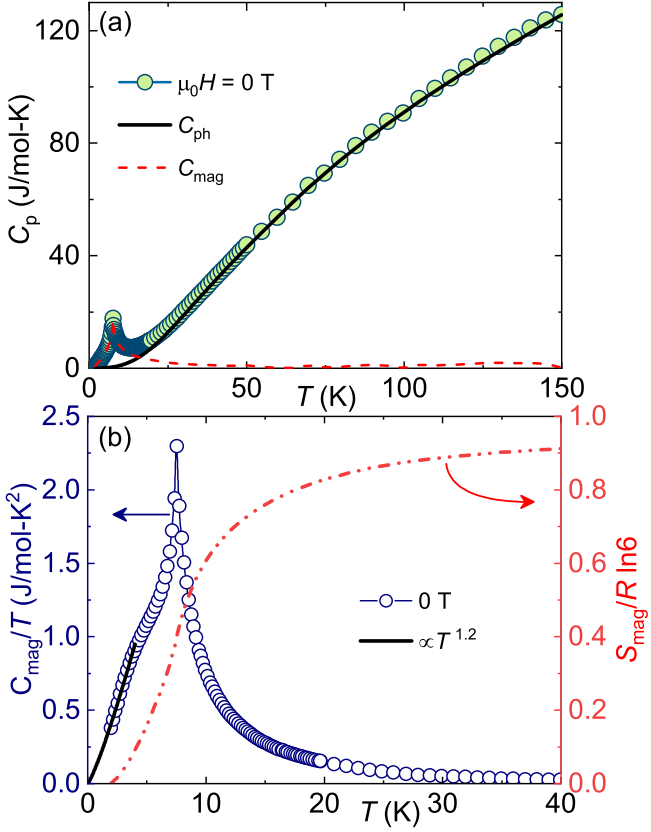


FIG. 7. (a) C_p vs T in zero field. The solid line denotes C_{ph} , while the dashed line represents C_{mag} . (b) C_{mag}/T and S_{mag} vs T in the left and right y -axes, respectively. The solid line is the power law fit to the C_{mag} data at low temperatures, below 3 K.

C. Heat capacity

Figure 7(a) shows the temperature dependence of heat capacity [$C_p(T)$] measured in zero-field. With decreasing temperature, $C_p(T)$ exhibits a pronounced λ -type anomaly at $T_{N1} \simeq 7.6$ K, signaling the onset of a magnetic LRO. No anomaly associated with T^* is observed in zero-field data.

In magnetic insulators, the total heat capacity can be expressed as $C_p(T) = C_{ph}(T) + C_{mag}(T)$, where the phonon contribution $C_{ph}(T)$ dominates at high temperatures, while the magnetic contribution $C_{mag}(T)$ dominates at low temperatures. To separate the two, we fitted $C_p(T)$ data using a Debye–Einstein model consisting of one Debye term and four Einstein terms [42, 43]:

$$C_{ph}(T) = f_D C_D(\theta_D, T) + \sum_{i=1}^4 g_i C_{E_i}(\theta_{E_i}, T), \quad (4)$$

where f_D and g_i are weight factors that satisfy $f_D + \sum g_i = 1$, consistent with the Dulong–Petit limit ($\sim 3nR$) at high temperatures [44]. The Debye term that accounts for the low-energy vibrations (acoustic modes)

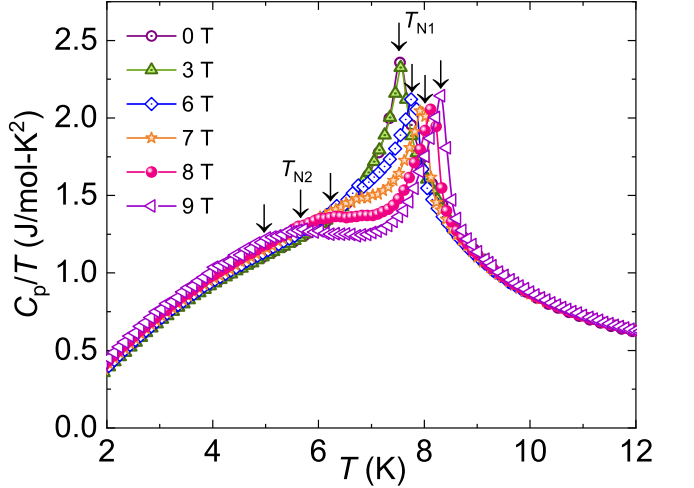


FIG. 8. C_p/T vs T in the low- T regime measured in different fields. The respective vertical arrows point to the transitions at T_{N1} and T_{N2} .

of heavy atoms can be written as

$$C_D(\theta_D, T) = 9nR \left(\frac{T}{\theta_D} \right)^3 \int_0^{\theta_D/T} \frac{x^4 e^x}{(e^x - 1)^2} dx. \quad (5)$$

The Einstein term describes the higher-energy optical modes and can be expressed as

$$C_E(\theta_E, T) = 3nR \left(\frac{\theta_E}{T} \right)^2 \frac{e^{\theta_E/T}}{(e^{\theta_E/T} - 1)^2}. \quad (6)$$

Here, θ_D and θ_E are the characteristic Debye and Einstein temperatures, respectively. The fit [solid line in Fig. 7(a)] in the high temperatures yields $f_D \simeq 0.079$, $g_1 \simeq 0.147$, $g_2 \simeq 0.255$, $g_3 \simeq 0.378$, $g_4 \simeq 0.141$, $\theta_D = 120(2)$ K, $\theta_{E_1} = 154(3)$ K, $\theta_{E_2} = 341(3)$ K, $\theta_{E_3} = 865(4)$ K, and $\theta_{E_4} = 1600(3)$ K. Subtracting $C_{ph}(T)$ from the measured $C_p(T)$ gives the magnetic part $C_{mag}(T)$, shown as the dashed line in Fig. 7(a).

Figure 7(b) presents $C_{mag}(T)/T$ vs T , which exhibits a sharp peak at T_{N1} along with a broad hump below it, typical of high-spin systems [16, 45]. Furthermore, the magnetic entropy was estimated as $S_{mag}(T) = \int_{1.95 \text{ K}}^T \frac{C_{mag}(T')}{T'} dT'$. The resulting entropy, plotted on the right y -axis of Fig. 7(b), saturates to a value $S_{mag} \simeq 13.85$ J/mol-K above 50 K, which is close to the expected value $R \ln(2S + 1) = 14.89$ J/mol-K for $S = 5/2$. At very low temperatures ($T < T_{N1}$), $C_{mag}(T)$ follows a power law with an exponent $\alpha \simeq 2.2$ which possibly reflects dominant 2D magnon excitation in the AFM ordered state [18, 46].

To access the field-induced transition, $C_p(T)$ in the low- T region measured in different fields is shown in Fig. 8. For $\mu_0 H \leq 6$ T, the transition at T_{N1} remains nearly unchanged. At higher fields ($\mu_0 H \geq 7$ T), an additional shoulder-like anomaly emerges at lower temperatures, which becomes more pronounced with increasing

field and is assigned to the field-induced transition T_{N2} . These findings are consistent with the $\chi(T)$ data. Similar behavior demonstrating field-induced transitions in specific heat is reported in other frustrated magnets and is generally attributed to the magnetic anisotropy [40, 41].

D. ^{31}P NMR

Nuclear magnetic resonance (NMR) is a powerful local probe for investigating both static and dynamic properties of correlated spin systems. Figure 1(a) illustrates the unit cell of RFHPO containing two crystallographically inequivalent $\text{HP}(1)\text{O}_3$ and $\text{HP}(2)\text{O}_3$ tetrahedra connected to the Fe^{3+} ions. As shown in Fig. 1(c), the Fe–Fe connectivity involves the pathway $\text{Fe}–\text{O}–\text{P}–\text{O}–\text{Fe}$. The structural analysis reveals the bond angles $\angle\text{Fe}–\text{P}(1)–\text{Fe} \simeq 115^\circ$ and $\angle\text{Fe}–\text{P}(2)–\text{Fe} \simeq 100^\circ$ and bond distances $\text{P}(1)–\text{Fe} \simeq 3.15 \text{ \AA}$ and $\text{P}(2)–\text{Fe} \simeq 3.45 \text{ \AA}$. Because of shorter bond distance and larger angle, one expects stronger hyperfine coupling for the P(1) site as compared to the P(2) site. Since the ^{31}P nuclei have a nuclear spin $I = 1/2$, each site is expected to produce a single resonance line in the paramagnetic regime.

1. ^{31}P NMR spectra ($T > T_{N1}$)

Figure 9 shows the field-swept ^{31}P NMR spectra measured at 120.6 MHz ($\mu_0 H \simeq 7 \text{ T}$) at different temperatures down to 9 K ($T > T_{N1}$). In the paramagnetic regime, two distinct resonance lines with finite asymmetry are observed, corresponding to the P1 and P2 sites. The presence of two inequivalent lines reflects different local magnetic environments, originating from site-dependent hyperfine interactions with Fe^{3+} moments. The broad line can be assigned to the strongly coupled P1 site, while the narrow line corresponds to the weakly coupled P2 site. The asymmetric line shape for both the P-sites can be attributed either to the asymmetry in hyperfine coupling or anisotropy in $\chi(T)$ [47, 48]. Upon cooling, both lines broaden and shift progressively towards lower magnetic fields.

To simulate the anisotropic powder spectra, we used the standard expression for the NMR shift (K)

$$K = K_{\text{iso}} + K_{\text{ax}}(3 \cos^2 \theta - 1), \quad (7)$$

where K_{iso} and K_{ax} denote the isotropic and axial components of the NMR shift, respectively, and θ is the angle between the applied magnetic field and the principal axis of the hyperfine tensor [49, 50]. A representative simulation of the spectrum at $T = 30 \text{ K}$ based on a two-site model, incorporating finite anisotropic shifts, is shown in the inset of Fig. 9. This approach was extended to other temperatures to extract the temperature dependence of K . It should be noted that at low temperatures just above T_{N1} , the NMR spectra were not reproduced well by

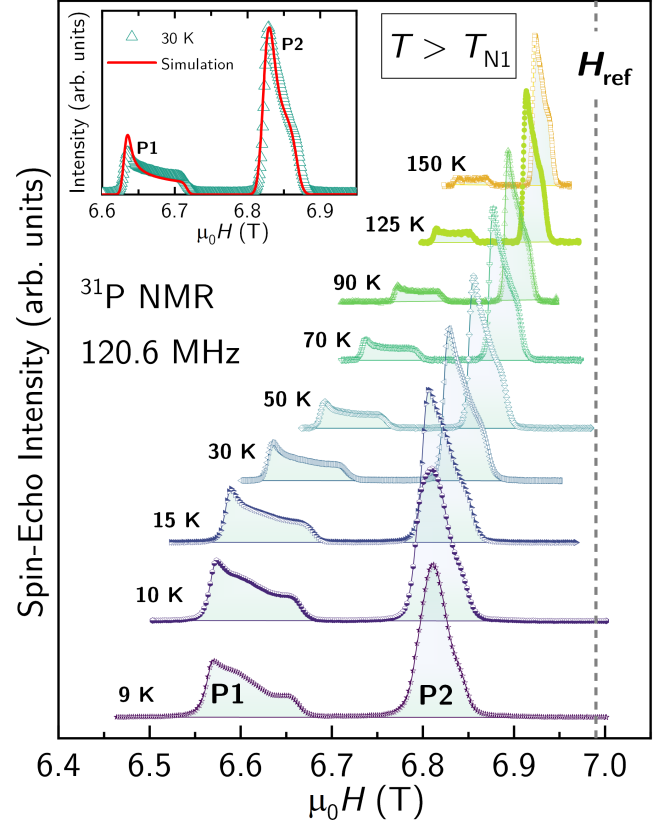


FIG. 9. Temperature-dependent field-swept ^{31}P NMR spectra measured at 120.6 MHz ($\mu_0 H \approx 7 \text{ T}$), down to 9 K ($T > T_{N1}$). The vertical dashed line marks the zero-shift position or reference field for ^{31}P nucleus. Inset: spectral simulation at $T = 30 \text{ K}$, accounting for the contributions from two inequivalent phosphorus sites (P1 and P2).

simulation, especially for the P1 site. This indicates that the P1 site has more than one environment with slightly different hyperfine coupling constants for unknown reasons, which produces the complicated NMR spectra in the magnetically ordered states.

The extracted $K_{\text{iso}}(T)$ and $K_{\text{ax}}(T)$ for both the P1 and P2 sites are plotted in Fig. 10(a) for two frequencies. Both the components of K are found to be frequency independent, as anticipated from the $\chi(T)$ data. With decreasing temperature, both the components of K increase, consistent with the Curie-Weiss behavior for $T > T_{N1}$. Since $K(T)$ reflects the intrinsic spin susceptibility $\chi_{\text{spin}}(T)$, it can be expressed as

$$K(T) = K_0 + \frac{A_{\text{hf}}}{N_A \mu_B} \chi_{\text{spin}}(T), \quad (8)$$

where K_0 is the temperature-independent chemical shift and A_{hf} is the hyperfine coupling constant between the ^{31}P nucleus and Fe^{3+} spins. In Fig. 10(b), K_{iso} and K_{ax} are plotted against χ measured at 7 T, with temperature as an implicit parameter. The observed linearity confirms that the NMR shift is tracking χ_{spin} , with no contribution from impurities or orphan spins. A linear fit yields

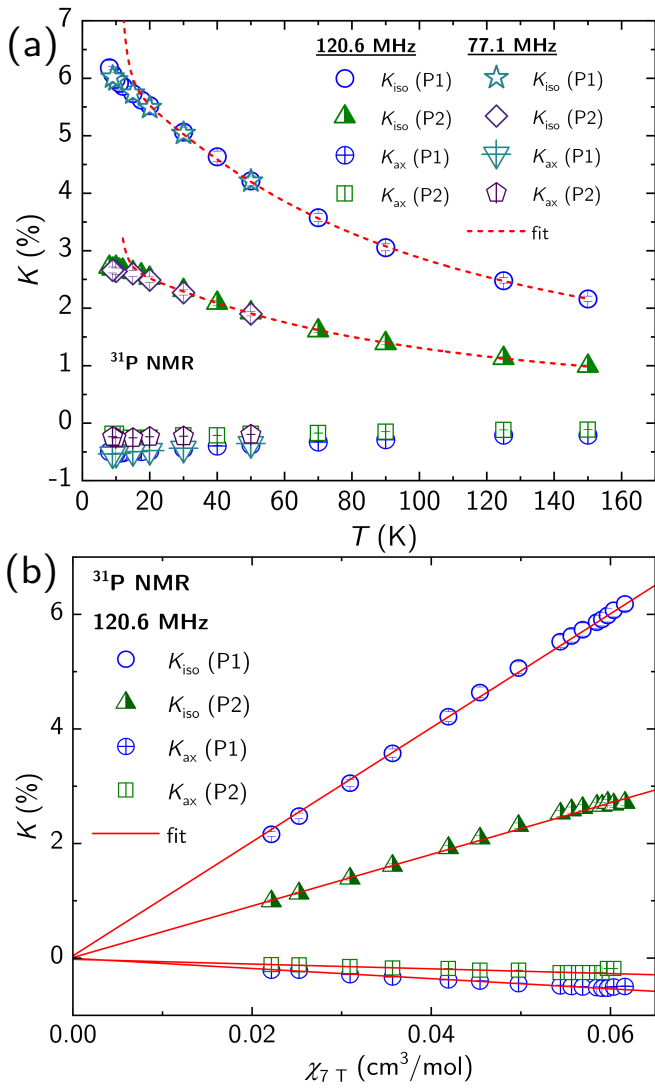


FIG. 10. (a) Temperature dependence of K_{iso} and K_{ax} for both P1 and P2 sites, measured at two different frequencies. The dashed curves represent the fits using Eq. (8) to $K_{\text{iso}}(T)$. (b) Clogston-Jaccarino plot of K_{iso} and K_{ax} vs χ with temperature as an implicit parameter. Solid lines represent linear fits.

the isotropic hyperfine coupling $A_{\text{hf}}^{\text{iso}} = 0.55(2) \text{ T}/\mu_{\text{B}}$ and $0.25(3) \text{ T}/\mu_{\text{B}}$ for the P1 and P2 sites, respectively. Similarly, the obtained axial hyperfine coupling is $A_{\text{hf}}^{\text{ax}} = -0.049(2) \text{ T}/\mu_{\text{B}}$ and $-0.023(1) \text{ T}/\mu_{\text{B}}$ for P1 and P2, respectively. These results indicate that P1 is strongly coupled to Fe^{3+} spins than P2, consistent with our site assignment based on the crystal structure. The obtained A_{hf} values are comparable to those reported in other phosphate-based AFMs [28, 47, 51].

Finally, the exchange coupling J/k_{B} between Fe^{3+} spins was estimated by fitting $K_{\text{iso}}(T)$ for both sites using Eq. (8), with $\chi_{\text{spin}}(T)$ given in Eq. (3). During the fit, $A_{\text{hf}}^{\text{iso}}$ was fixed to the values obtained from the $K - \chi$ analysis. As shown in Fig. 10(a), the fits above 15 K for

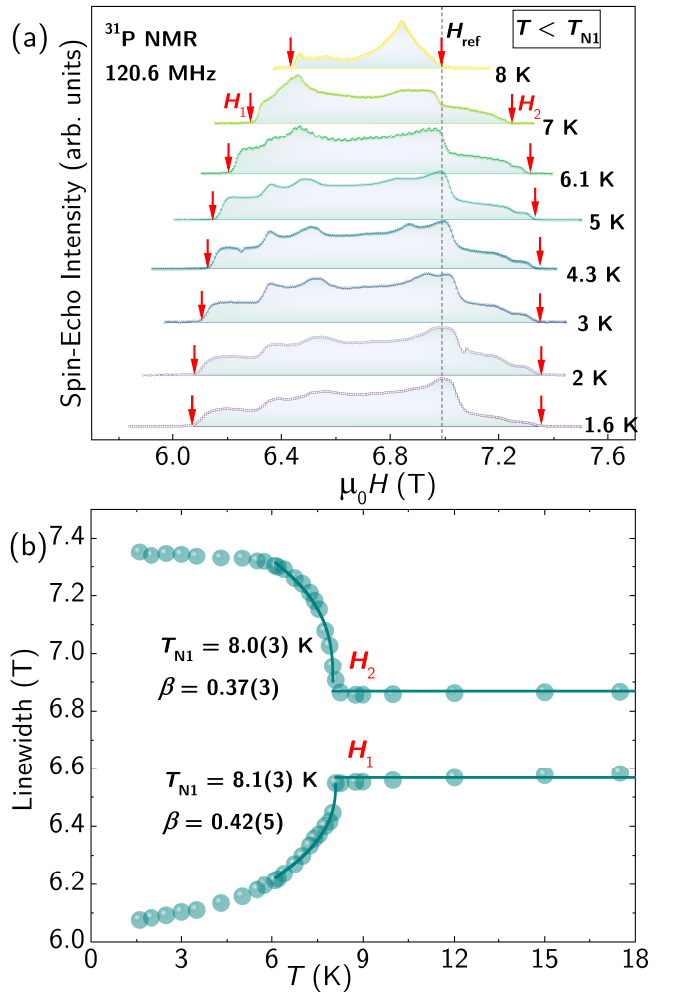


FIG. 11. (a) ^{31}P NMR spectra measured below 9 K at 120.6 MHz. The vertical dashed line corresponds to ^{31}P zero-shift position. The downward arrows indicate the low- H and high- H edges of the NMR spectra. (b) Temperature dependence of the low- and high- H edge positions (H_1 and H_2) of the NMR spectra. The dark solid lines are fitting results using Eq. (9) in the critical regime.

both the sites yield $J/k_{\text{B}} = 2.6(2) \text{ K}$ and $g = 2.01(1)$, which are in good agreement with the $\chi(T)$ analysis.

2. ^{31}P NMR spectra ($T < T_{\text{N1}}$)

Figure 11(a) shows the low temperature ^{31}P NMR spectra at 120.6 MHz. Below $T_{\text{N1}} \simeq 8 \text{ K}$, the spectra broaden markedly and the two lines observed in the paramagnetic state merge into a single, broad, and anisotropic line. This rapid broadening signals the development of a static internal field at the ^{31}P sites as the system enters the magnetic ordered state. At low temperatures, the spectra evolve into a nearly rectangular shape with multiple features. Such a rectangular pattern is a characteristic feature of a commensurate AFM state which arises

due to the random orientation of internal hyperfine fields with respect to the external field in a polycrystalline sample [51–54]. The features in our NMR spectra below T_{N1} evolve systematically with more number of shoulders as the temperature is lowered. No clear features could be assigned solely to T_{N2} expected from $\chi(T)$ and $C_p(T)$.

In general, as the broadening of the lines is due to the static internal field at the P sites produced by the ordered Fe moments, the temperature dependence of the linewidth reflects that of the sublattice magnetization (i.e., the order parameter) in the magnetically ordered state. However, as described above, the observed spectra exhibit a complex shape due to the two inequivalent P sites, as well as the additional P1 site with a slightly different hyperfine coupling. As a result, it is not straightforward to extract the temperature dependence of the static internal field from the spectra. Therefore, we tracked the temperature dependence of the low- and high-magnetic field edge positions of the spectra [H_1 and H_2 , indicated by the arrows in Fig. 11(a)]. Assuming the low-field edge originates from the internal field at the P1 site ($H_{\text{int},\text{P1}}$), H_1 can be written as $H_1(T) = H_{0,\text{P1}} - H_{\text{int},\text{P1}}(T)$, where $H_{0,\text{P1}}$ is the center position for the P1 line. Similarly, since the high-field edge H_2 most likely arises from the P2 line, one can express it as $H_2(T) = H_{0,\text{P2}} + H_{\text{int},\text{P2}}(T)$, where $H_{\text{int},\text{P2}}$ is the internal field at P2 and $H_{0,\text{P2}}$ is the center position of the P2 line. The temperature dependencies of H_1 and H_2 are shown in Fig. 11(b). Notably, H_1 and H_2 exhibit different temperature dependence: H_2 nearly saturates below ~ 5 K, whereas H_1 keeps decreasing down to the lowest temperature measured. This indicates that $H_{0,\text{P1}}$ and $H_{0,\text{P2}}$ are not strictly temperature independent but decrease slightly with decreasing temperature. Nevertheless, we used the data to extract the critical exponent of the order parameter and fitted the data by a power-law of the following form near T_{N1} (critical regime) assuming $H_{0,\text{P1}}$ and $H_{0,\text{P2}}$ are effectively constant in the limited regime:

$$H_i(T) = H_{0,\text{Pi}} \mp H_{\text{int},\text{Pi}}(0) \left(1 - \frac{T}{T_{N1}}\right)^\beta. \quad (9)$$

Here, β is the critical exponent of the order parameter and $i = 1$ and 2 with minus or plus signs in the formula, respectively. The fits in the range 6.1 - 8.1 K yields $\beta = 0.42(5)$, $H_{\text{int},\text{P1}}(0) = 0.59$ T, $T_{N1} = 8.1(3)$ K, and $H_{0,\text{P1}} \simeq 6.55$ T for P1, and $\beta = 0.37(3)$, $H_{\text{int},\text{P2}}(0) = 0.70$ T, $T_{N1} = 8.0(3)$ K, and $H_{0,\text{P2}} \simeq 6.90$ T for P2, respectively. The slight different values of β are due to the temperature dependence of $H_{0,\text{P1}}$ and $H_{0,\text{P2}}$ and are considered to be possible upper and lower values. Because these values are close to those expected for a 3D AFM [51, 55] and significantly greater than those expected for 2D AFM systems (0.125 for Ising model and 0.231 for XY model) [56–58], the results suggest a 3D AFM nature of RFHPO.

3. ^{31}P spin-lattice relaxation rate ($1/T_1$)

To probe the local spin dynamics, we measured the temperature-dependent ^{31}P spin-lattice relaxation rate ($1/T_1$) down to 9 K at the central peak positions of both the P1 and P2 sites and at two frequencies 120.6 MHz ($\mu_0 H \approx 7$ T) and 77.1 MHz ($\mu_0 H \approx 4.5$ T). However, for $T < 9$ K, since the line is very broad and two P-sites are merged, we measured $1/T_1$ at the extreme left and right shoulder positions. The values of $1/T_1$ at both the shoulder positions are found to be the same. For a nucleus with spin $I = 1/2$, the recovery of the longitudinal magnetization typically follows a single exponential function. In the present case, the recovery curves are best described by a stretched exponential

$$1 - \frac{M(t)}{M(\infty)} = A e^{-(t/T_1)^\beta}, \quad (10)$$

where $M(t)$ and $M(\infty)$ are the nuclear magnetizations at time t and at equilibrium, respectively, and β is the stretch exponent. Above T_{N1} , the recovery is single-exponential with $\beta = 1$, while at T_{N1} the value of β drops suddenly and saturates to $\beta \simeq 0.8$ [see inset of Fig. 12(b)]. This suggests a distribution of relaxation time below T_{N1} [28].

Figure 12(b) presents the temperature dependence of $1/T_1$ for both P-sites. In the paramagnetic regime, the two P-sites exhibit distinct $1/T_1$ values due to their different hyperfine couplings. Above ~ 15 K, $1/T_1$ remains nearly constant, reflecting localized paramagnetic fluctuations. On approaching T_{N1} , $1/T_1$ exhibits a sharp peak at both fields, evidencing critical slowing down of spin fluctuations near the magnetic ordering [43]. This value of $T_{N1} \simeq 8$ K is consistent with the $\chi(T)$ and $C_p(T)$ results. Below T_{N1} , $1/T_1$ decreases rapidly, and at low- T s it follows a T^3 dependence, consistent with the two-magnon Raman process, as reported in other TLAJs [51]. In contrast to the $\chi(T)$ and $C_p(T)$ data, the field-induced transition at T_{N2} is not manifested in NMR $1/T_1(T)$.

The divergent behaviour of $1/T_1$ near T_{N1} reflects critical fluctuations associated with a second-order transition. To analyze this behavior, we plotted $1/T_1$ versus reduced temperature $\epsilon = (T - T_{N1})/T_{N1}$ in Fig. 12(c). A power-law fit yields the critical exponent $\sim 0.28(3)$ and $\sim 0.58(3)$ for the P1 and P2 sites, respectively. Compared to the P1 site, the P2 site shows more clear critical behavior. The critical exponent value $\sim 0.56(5)$ for the P2 site is close to the expected value (~ 0.6) for 3D Ising universality class [59], whereas the smaller exponent for P1 may arise from a smaller form-factor. The smaller form-factor for P1 can also be inferred based on the observation that the $H_{\text{int},\text{P1}}$ is slightly smaller than $H_{\text{int},\text{P2}}$ as shown above. Since the hyperfine coupling constant A_{hf} for P1 is twice as that for P2, the smaller internal magnetic field must stem from a smaller form-factor in P1. Similar behaviors have been observed in iron-based superconductors $\text{CaK}(\text{Fe}_{1-x}\text{Ni}_x)_4\text{As}_4$ in which distinct

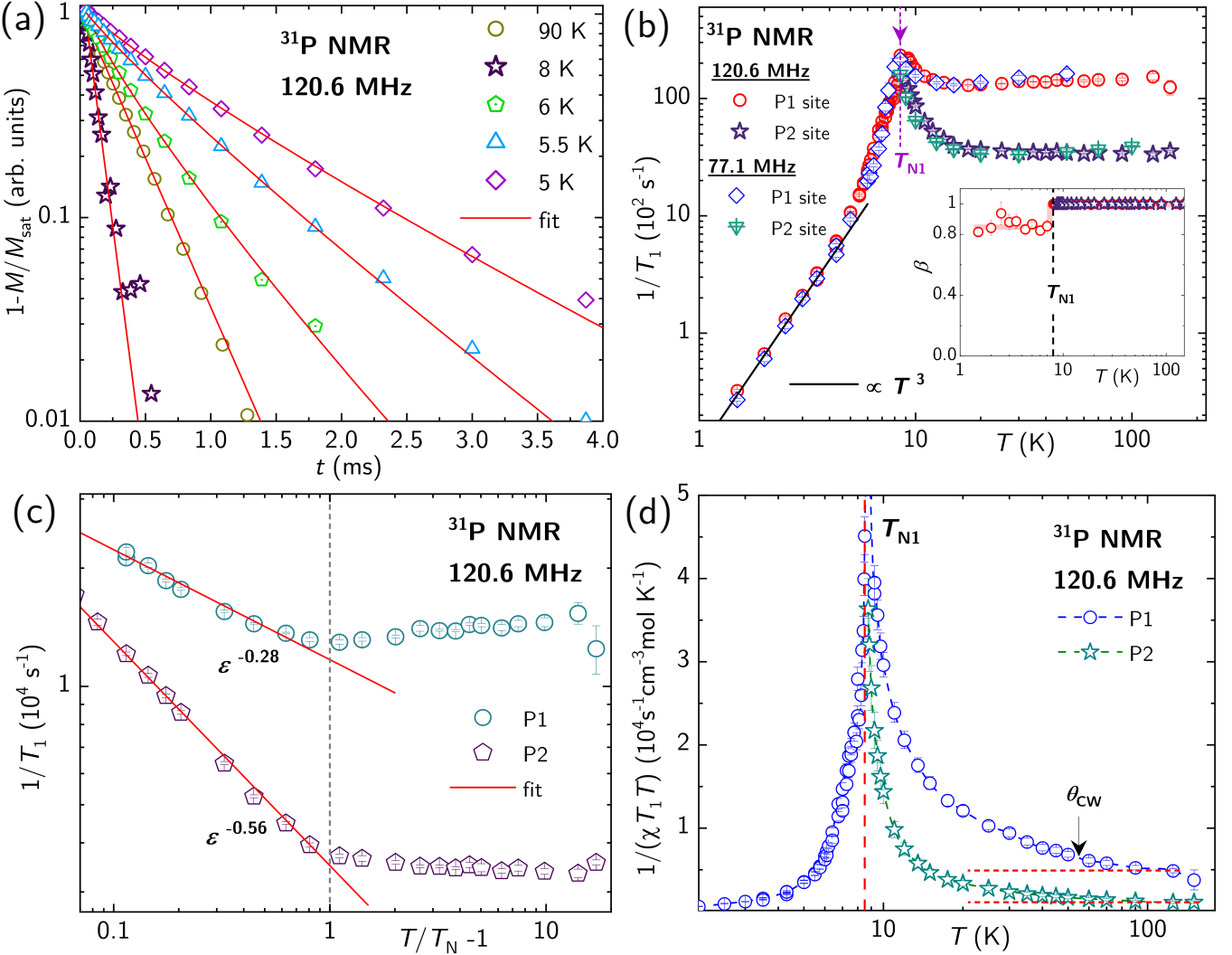


FIG. 12. (a) Recovery of the longitudinal nuclear magnetization at 120.6 MHz measured at the P1 site. Solid lines are fits using Eq. (10). (b) Temperature dependence of the ^{31}P $1/T_1$ measured at 120.6 MHz and 77.1 MHz for both P1 and P2 sites. The downward arrow indicates T_{N1} . Solid line below T_{N1} represent T^3 fit. Inset: temperature dependence of exponent (β) for both P1 and P2 sites. (c) $1/T_1$ plotted as a function of reduced temperature $\epsilon \equiv (T/T_{N1} - 1)$ for both P-sites. Solid lines are the power-law fits in the critical regime. (d) Temperature dependence of $1/(\chi T_1 T)$. The horizontal dotted lines mark the constant behaviour at high temperatures and the vertical dash-dotted line denotes T_{N1} .

critical fluctuations were observed at different As sites due to different form factors [60–62].

To probe the nature of spin fluctuations in the paramagnetic regime (above T_N), we analyzed the temperature dependence of $1/(\chi T_1 T)$, as presented in Fig. 12(d). At high temperatures, $1/(\chi T_1 T)$ remains nearly constant, while it shows a gradual increase below ~ 60 K. The nuclear spin-lattice relaxation rate divided by temperature, $\frac{1}{T_1 T}$, is related to the imaginary part of the dynamical spin susceptibility $\chi_M''(\vec{q}, \omega_N)$ at the NMR frequency ω_N through the relation [63]

$$\frac{1}{T_1 T} = \frac{2\gamma_N^2 k_B}{N_A^2} \sum_{\vec{q}} |A(\vec{q})|^2 \frac{\chi_M''(\vec{q}, \omega_N)}{\omega_N}, \quad (11)$$

where the summation extends over all wave vectors \vec{q} in the first Brillouin zone, and $A(\vec{q})$ denotes the hyperfine form factor. For $q = 0$ and $\omega_N = 0$, the real part of $\chi_M(\vec{q}, \omega_N)$ corresponds to the uniform static susceptibility (χ). Therefore, the temperature-independent behavior of $1/(\chi T_1 T)$ in the high-temperature region ($T > \theta_{CW}$) implies that $1/T_1 T$ is mainly governed by the uniform susceptibility χ . The mild upturn below ~ 60 K signifies the development of spin correlations with $q \neq 0$ or short-range AFM fluctuations, as typically observed in low-dimensional frustrated spin systems [55].

IV. DISCUSSION AND SUMMARY

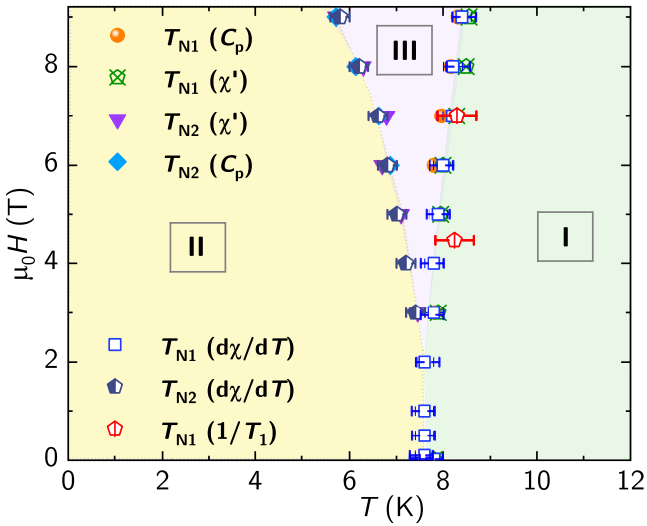


FIG. 13. The $H - T$ phase diagram highlighting the evolution of T_{N1} and T_{N2} with H , obtained from the dc and ac susceptibility, heat capacity, and NMR measurements. For dc susceptibility, the transition temperatures are determined by plotting the temperature derivative. Three distinct phases are marked as (I), (II), and (III).

The $H - T$ phase diagram of RFHPO presented in Fig. 13 has been constructed using transition temperatures from $\chi(T)$, $\chi'(T)$, $C_p(T)$, and $1/T_1(T)$. Three regimes are identified as: (I) high-temperature paramagnetic state, (II) an AFM ordered state, and (III) a field-induced phase. In zero-field, the system undergoes a single transition at $T_{N1} \simeq 7.8$ K into a commensurate AFM state, as confirmed by the rectangular NMR line-shape. Remarkably, T_{N1} shifts to higher temperatures for $\mu_0 H > 3$ T, a contrasting behaviour expected for a conventional AFM. Typically, this unusual increase can possibly be attributed to the interplay of AFM LRO and quantum fluctuations. In low-dimensional and frustrated magnets, quantum fluctuations usually suppress the magnetic LRO. In RFHPO, when magnetic field is applied, a small field partially quenches/weaken these fluctuations; as a result, T_{N1} is shifted towards high temperatures. In higher fields, it is expected to shift back to low temperatures. A similar field-driven shift of the transition temperature has been observed in other high-spin frustrated TLAfs, such as $\text{Ba}_3\text{MnNb}_2\text{O}_9$, $\text{NH}_4\text{Fe}(\text{PO}_3\text{F})_2$, and $\text{Rb}_4\text{Mn}(\text{MoO}_4)_3$ [13, 28, 40]. For $\mu_0 H > 3$ T, an additional transition T_{N2} emerges, giving rise to the intermediate regime (III). Unlike T_{N1} , T_{N2} shifts to low temperatures with increasing field, consistent with a conventional AFM nature. Clearly, there are at least two magnetic phases (II and III) that possess different spin reorientations. Therefore, we presume that this unusual phase boundary separating II and III could be due to magnetic anisotropy, which induces spin canting and hence, the

complex phase diagram, akin to the behavior reported in several TLAfs [9, 13, 64].

In an ideal 2D Heisenberg TLAf, the ground state in zero-field is a non-collinear 120° structure [10]. Under applied fields, quantum fluctuations and interlayer couplings lift the degeneracy, stabilizing distinct spin configurations. A particularly interesting example is the stabilization of a collinear up-up-down (uud) state by the magnetic field, which is manifested as a $1/3$ magnetization plateau [65]. Indeed, such a plateau has been experimentally observed in several TLAfs ranging from low-spin ($S = 1/2$) to high-spin cases [66, 67]. In principle, the large spin ($S = 5/2$) and weak anisotropy of Fe^{3+} ions should still allow for the stabilization of a field-induced $1/3$ plateau in RFHPO. However, since the expected saturation field ($\mu_0 H_{\text{sat}} \simeq 50$ T) of RFHPO is very high, probing this $1/3$ plateau would require high magnetic fields, which is beyond the field range of our present experiments.

In summary, we have presented a comprehensive study of thermodynamic, static, and dynamic properties of $\text{RbFe}(\text{HPO}_3)_2$. The compound features equilateral triangular layers of Fe^{3+} ($S = 5/2$) ions stacked along the c -axis. Our analysis of $\chi(T)$ and $K_{\text{iso}}(T)$ validates the Heisenberg TLAf model with an average exchange coupling of $J/k_B \simeq 2.8$ K. It undergoes a magnetic ordering at $T_{N1} \simeq 7.8$ K in zero-field, characterized by a distinct anomaly in $\chi(T)$, $C_p(T)$, and $1/T_1(T)$. The ^{31}P NMR spectra reveal two inequivalent phosphorus sites and the $K-\chi$ analysis yields isotropic hyperfine couplings of $A_{\text{hf}}^{\text{iso}} = 0.55(2)$ T/ μ_B and $0.25(3)$ T/ μ_B for the P1 and P2 sites, respectively. The NMR spectra further confirm a commensurate antiferromagnetic ordering below T_{N1} . While the thermodynamic measurements establish a field-induced transition at T_{N2} , this feature is absent in the $1/T_1(T)$ data. The resulting $H^\sim - T$ phase diagram highlights the delicate competition between frustration, anisotropy, and dimensionality in stabilizing multiple distinct magnetic phases. Further studies on high-quality single crystals are essential to resolve the ambiguity about the field-induced transition at T_{N2} , spin structures, and possible magnetization plateaus in this compound.

ACKNOWLEDGMENTS

VN, SJS, SPP, and RN acknowledge SERB, India, for financial support bearing sanction Grant No. CRG/2022/000997 and DST-FIST with Grant No. SR/FST/PS-II/2018/54(C). SJS acknowledges the Fulbright-Nehru Doctoral Research Fellowship Award No. 2997/FNDR/2024-2025 and the Prime Minister's Research Fellowship (PMRF) scheme, Government of India, to be a visiting research scholar at the Ames National Laboratory. The research was supported by the US Department of Energy, Office of Basic Energy Sciences, Division of Materials Sciences and Engineering.

Ames National Laboratory is operated for the US De-

partment of Energy by Iowa State University under Contract No. DEAC02-07CH11358.

[1] H. T. Diep, *Frustrated Spin Systems*, 2nd ed. (WORLD SCIENTIFIC, 2013).

[2] P. Anderson, Resonating valence bonds: A new kind of insulator?, *Mater. Res. Bull.* **8**, 153 (1973).

[3] L. Balents, Spin liquids in frustrated magnets, *Nature* **464**, 199 (2010).

[4] T. Jolicoeur and J. C. Le Guillou, Spin-wave results for the triangular Heisenberg antiferromagnet, *Phys. Rev. B* **40**, 2727 (1989).

[5] A. V. Chubukov, S. Sachdev, and T. Senthil, Large-S expansion for quantum antiferromagnets on a triangular lattice, *J. Phys. Condens. Matter.* **6**, 8891 (1994).

[6] A. I. Smirnov, L. E. Svitov, L. A. Prozorova, A. Zheludev, M. D. Lumsden, E. Ressouche, O. A. Petrenko, K. Nishikawa, S. Kimura, M. Hagiwara, K. Kindo, A. Y. Shapiro, and L. N. Demianets, Chiral and collinear ordering in a distorted triangular antiferromagnet, *Phys. Rev. Lett.* **102**, 037202 (2009).

[7] C. A. Gallegos, S. Jiang, S. R. White, and A. L. Chernyshev, Phase Diagram of the Easy-Axis Triangular-Lattice J_1-J_2 Model, *Phys. Rev. Lett.* **134**, 196702 (2025).

[8] P.-E. Melchy and M. E. Zhitomirsky, Interplay of anisotropy and frustration: Triple transitions in a triangular-lattice antiferromagnet, *Phys. Rev. B* **80**, 064411 (2009).

[9] L. Seabra, T. Momoi, P. Sindzingre, and N. Shannon, Phase diagram of the classical heisenberg antiferromagnet on a triangular lattice in an applied magnetic field, *Phys. Rev. B* **84**, 214418 (2011).

[10] M. F. Collins and O. A. Petrenko, Review/synthèse: Triangular antiferromagnets, *Can. J. Phys.* **75**, 605 (1997).

[11] H. Kadowaki, K. Ubukoshi, and K. Hirakawa, Neutron Scattering Study of Successive Phase Transitions in Triangular Lattice Antiferromagnet CsNiCl_3 , *J. Phys. Soc. Jpn* **56**, 751 (1987).

[12] Y. Doi, Y. Hinatsu, and K. Ohoyama, Structural and magnetic properties of pseudo-two-dimensional triangular antiferromagnets $\text{Ba}_3\text{MSb}_2\text{O}_9$ ($\text{M} = \text{Mn, Co, and Ni}$), *J. Phys. Condens. Matter.* **16**, 8923 (2004).

[13] M. Lee, E. S. Choi, X. Huang, J. Ma, C. R. Dela Cruz, M. Matsuda, W. Tian, Z. L. Dun, S. Dong, and H. D. Zhou, Magnetic phase diagram and multiferroicity of $\text{Ba}_3\text{MnNb}_2\text{O}_9$: A spin- $\frac{5}{2}$ triangular lattice antiferromagnet with weak easy-axis anisotropy, *Phys. Rev. B* **90**, 224402 (2014).

[14] K. M. Ranjith, K. Brinda, U. Arjun, N. G. Hegde, and R. Nath, Double phase transition in the triangular antiferromagnet $\text{Ba}_3\text{CoTa}_2\text{O}_9$, *J. Phys.: Condens. Matter* **29**, 115804 (2017).

[15] S. Lal, S. J. Sebastian, S. S. Islam, M. P. Saravanan, M. Uhlazar, Y. Skourski, and R. Nath, Double magnetic transitions and exotic field-induced phase in the triangular lattice antiferromagnets $\text{Sr}_3\text{Co}(\text{Nb, Ta})_2\text{O}_9$, *Phys. Rev. B* **108**, 014429 (2023).

[16] S. J. Sebastian, S. S. Islam, A. Jain, S. M. Yusuf, M. Uhlazar, and R. Nath, Collinear order in the spin- $\frac{5}{2}$ triangular-lattice antiferromagnet $\text{Na}_3\text{Fe}(\text{PO}_4)_2$, *Phys. Rev. B* **105**, 104425 (2022).

[17] K. Bhattacharya, S. Mohanty, A. D. Hillier, M. T. F. Telling, R. Nath, and M. Majumder, Evidence of quantum spin liquid state in a Cu^{2+} -based $S = \frac{1}{2}$ triangular lattice antiferromagnet, *Phys. Rev. B* **110**, L060403 (2024).

[18] K. Somesh, Y. Furukawa, G. Simutis, F. Bert, M. Prinz-Zwick, N. Büttgen, A. Zorko, A. A. Tsirlin, P. Mendels, and R. Nath, Universal fluctuating regime in triangular chromate antiferromagnets, *Phys. Rev. B* **104**, 104422 (2021).

[19] H. Serrano-González, S. T. Bramwell, K. D. M. Harris, B. M. Kariuki, L. Nixon, I. P. Parkin, and C. Ritter, Magnetic structures of the triangular lattice magnets $\text{AFe}(\text{SO}_4)_2$ ($\text{A} = \text{K, Rb, Cs}$), *J. Appl. Phys.* **83**, 6314 (1998).

[20] T. Inami, Y. Ajiro, and T. Goto, Magnetization Process of the Triangular Lattice Antiferromagnets, $\text{RbFe}(\text{MoO}_4)_2$ and $\text{CsFe}(\text{SO}_4)_2$, *J. Phys. Soc. Jpn.* **65**, 2374 (1996).

[21] G. Nilsen, A. Raja, A. Tsirlin, H. Mutka, D. Kasinathan, C. Ritter, and H. Rønnow, One-dimensional quantum magnetism in the anhydrous alum $\text{KTi}(\text{SO}_4)_2$, *New J. Phys.* **17**, 113035 (2015).

[22] L. E. Svitov, A. I. Smirnov, L. A. Prozorova, O. A. Petrenko, A. Y. Shapiro, and L. N. Dem'yanets, On the possible coexistence of spiral and collinear structures in antiferromagnetic $\text{KFe}(\text{MoO}_4)_2$, *JETP Lett.* **80**, 204 (2004).

[23] L. E. Svitov, A. I. Smirnov, L. A. Prozorova, O. A. Petrenko, L. N. Demianets, and A. Y. Shapiro, Quasi-two-dimensional antiferromagnet on a triangular lattice $\text{RbFe}(\text{MoO}_4)_2$, *Phys. Rev. B* **67**, 094434 (2003).

[24] H. Mitamura, R. Watanuki, K. Kaneko, N. Onozaki, Y. Amou, S. Kittaka, R. Kobayashi, Y. Shimura, I. Yamamoto, K. Suzuki, S. Chi, and T. Sakakibara, Spin-Chirality-Driven Ferroelectricity on a Perfect Triangular Lattice Antiferromagnet, *Phys. Rev. Lett.* **113**, 147202 (2014).

[25] A. H. Abdeldaim, D. I. Badrtdinov, A. S. Gibbs, P. Manuel, H. C. Walker, M. D. Le, C. H. Wu, D. Wardecki, S.-G. Eriksson, Y. O. Kvashnin, A. A. Tsirlin, and G. J. Nilsen, Large easy-axis anisotropy in the one-dimensional magnet $\text{BaMo}(\text{PO}_4)_2$, *Phys. Rev. B* **100**, 214427 (2019).

[26] L. E. Svitov, A. I. Smirnov, L. A. Prozorova, O. A. Petrenko, A. Micheler, N. Büttgen, A. Y. Shapiro, and L. N. Demianets, Magnetic phase diagram, critical behavior, and two-dimensional to three-dimensional crossover in the triangular lattice antiferromagnet $\text{RbFe}(\text{MoO}_4)_2$, *Phys. Rev. B* **74**, 024412 (2006).

[27] S. Siebeneichler, K. V. Dorn, A. Ovchinnikov, W. Pawassiliou, I. da Silva, V. Smetana, A. J. Pell, and A.-V. Mudring, Frustration and 120° Magnetic Ordering in the Layered Triangular Antiferromagnets $\text{AFe}(\text{PO}_3\text{F})_2$ ($\text{A} = \text{K, (NH}_4\text{)}_2\text{Cl, NH}_4$, Rb, and Cs), *Chem. Mater.* **34**, 7982 (2022).

[28] S. Mohanty, K. M. Ranjith, C. S. Saramgi, Y. Skourski, B. Büchner, H.-J. Grafe, and R. Nath, Ground-state properties of the spin- $\frac{5}{2}$ frustrated triangular lattice antiferromagnet $\text{NH}_4\text{Fe}(\text{PO}_3\text{F})_2$, *Phys. Rev. B* **111**, 184435 (2025).

[29] F. Hamchaoui, V. Alonzo, D. Venegas-Yazigi, H. Rebbah, and E. Le Fur, Six novel transition-metal phosphite compounds, with structure related to yavapaiite: Crystal structures and magnetic and thermal properties of $A^I[M^{III}(\text{HPO}_3)_2]$ ($A = \text{K}, \text{NH}_4, \text{Rb}$ and $M = \text{V}, \text{Fe}$), *J. Sol. State Chem.* **198**, 295 (2013).

[30] S. Todo and K. Kato, Cluster Algorithms for General- S Quantum Spin Systems, *Phys. Rev. Lett.* **87**, 047203 (2001).

[31] A. Albuquerque, F. Alet, P. Corboz, P. Dayal, A. Feiguin, S. Fuchs, L. Gamper, E. Gull, S. Gürtler, A. Honecker, R. Igarashi, M. Körner, A. Kozhevnikov, A. Läuchli, S. Manmana, M. Matsumoto, I. McCulloch, F. Michel, R. Noack, G. Pawłowski, L. Pollet, T. Pruschke, U. Schollwöck, S. Todo, S. Trebst, M. Troyer, P. Werner, and S. Wessel, The ALPS project release 1.3: Open-source software for strongly correlated systems, *J. Magn. Magn. Mater.* **310**, 1187 (2007).

[32] G. A. Bain and J. F. Berry, Diamagnetic corrections and pascal's constants, *J. Chem. Edu.* **85**, 532 (2008).

[33] C. Domb and A. Miedema, Chapter VI Magnetic Transitions, *Prog. Low Temp. Phys.* **4**, 296 (1964).

[34] H. Kawamura and S. Miyashita, Phase Transition of the Heisenberg Antiferromagnet on the Triangular Lattice in a Magnetic Field, *J. Phys. Soc. Jpn.* **54**, 4530 (1985).

[35] C. Delmas, G. Le Flem, C. Fouassier, and P. Hagenmuller, Etude comparative des propriétés magnétiques des oxydes lamellaires ACrO_2 ($A = \text{Li}, \text{Na}, \text{K}$)^{-II}: Calcul des intégrales d'échange, *J. Phys. Chem. Sol.* **39**, 55 (1978).

[36] H.-J. Schmidt, A. Lohmann, and J. Richter, Eighth-order high-temperature expansion for general Heisenberg Hamiltonians, *Phys. Rev. B* **84**, 104443 (2011).

[37] V. B. Nalbandyan, E. A. Zvereva, A. Y. Nikulin, I. L. Shuklaev, M.-H. Whangbo, H.-J. Koo, M. Abdel-Hafiez, X.-J. Chen, C. Koo, A. N. Vasiliev, and R. Klingeler, New Phase of MnSb_2O_6 Prepared by Ion Exchange: Structural, Magnetic, and Thermodynamic Properties, *Inorg. Chem.* **54**, 1705 (2015).

[38] A. Ghosh, K.-H. Chen, X.-S. Qiu, S. H. Hsieh, Y. C. Shao, C. H. Du, H. T. Wang, Y. Y. Chin, J. W. Chiou, S. C. Ray, H. M. Tsai, C. W. Pao, H. J. Lin, J. F. Lee, R. Sankar, F. C. Chou, and W. F. Pong, Anisotropy in the magnetic interaction and lattice-orbital coupling of single crystal Ni_3TeO_6 , *Sci. Rep.* **8**, 15779 (2018).

[39] R. Nath, K. M. Ranjith, J. Sichelschmidt, M. Baenitz, Y. Skourski, F. Alet, I. Rousochatzakis, and A. A. Tsirlin, Hindered magnetic order from mixed dimensionalities in CuP_2O_6 , *Phys. Rev. B* **89**, 014407 (2014).

[40] R. Ishii, S. Tanaka, K. Onuma, Y. Nambu, M. Tokunaga, T. Sakakibara, N. Kawashima, Y. Maeno, C. Broholm, D. P. Gauthreaux, J. Y. Chan, and S. Nakatsuji, Successive phase transitions and phase diagrams for the quasi-two-dimensional easy-axis triangular antiferromagnet $\text{Rb}_4\text{Mn}(\text{MoO}_4)_3$, *Europhys. Lett.* **94**, 17001 (2011).

[41] L. Yue, Z. Lu, K. Yan, L. Wang, S. Guo, R. Guo, P. Chen, X. Chen, and J.-W. Mei, Magnetic phase transitions in the triangular-lattice spin-1 dimer compound $\text{K}_2\text{Ni}_2(\text{SeO}_3)_3$, *Phys. Rev. B* **109**, 214430 (2024).

[42] E. Gopal, *Specific Heats at Low Temperatures*, The International Cryogenics Monograph Series (Springer US, 2012).

[43] S. J. Sebastian, K. Somesh, M. Nandi, N. Ahmed, P. Bag, M. Baenitz, B. Koo, J. Sichelschmidt, A. A. Tsirlin, Y. Furukawa, and R. Nath, Quasi-one-dimensional magnetism in the spin- $\frac{1}{2}$ antiferromagnet $\text{BaNa}_2\text{Cu}(\text{VO}_4)_2$, *Phys. Rev. B* **103**, 064413 (2021).

[44] R. K. Fitzgerel and F. H. Verhoek, The law of Dulong and Petit, *J. Chem. Edu.* **37**, 545 (1960).

[45] R. Nath, K. M. Ranjith, B. Roy, D. C. Johnston, Y. Furukawa, and A. A. Tsirlin, Magnetic transitions in the spin- $\frac{5}{2}$ frustrated magnet BiMn_2PO_6 and strong lattice softening in BiMn_2PO_6 and BiZn_2PO_6 below 200 K, *Phys. Rev. B* **90**, 024431 (2014).

[46] H. Takatsu, H. Yoshizawa, S. Yonezawa, and Y. Maeno, Critical behavior of the metallic triangular-lattice Heisenberg antiferromagnet PdCrO_2 , *Phys. Rev. B* **79**, 104424 (2009).

[47] S. S. Islam, K. M. Ranjith, M. Baenitz, Y. Skourski, A. A. Tsirlin, and R. Nath, Frustration of square cupola in $\text{Sr}(\text{TiO})\text{Cu}_4(\text{PO}_4)_4$, *Phys. Rev. B* **97**, 174432 (2018).

[48] A. Yogi, N. Ahmed, R. Nath, A. A. Tsirlin, S. Kundu, A. V. Mahajan, J. Sichelschmidt, B. Roy, and Y. Furukawa, Antiferromagnetism of $\text{Zn}_2\text{VO}(\text{PO}_4)_2$ and the dilution with Ti^{4+} , *Phys. Rev. B* **91**, 024413 (2015).

[49] C. P. Slichter, *Principles of magnetic resonance*, Vol. 1 (Springer Science & Business Media, 2013).

[50] S. J. Sebastian, R. Kolay, A. B. Q.-P. Ding, Y. Furukawa, and R. Nath, Spin fluctuations, absence of magnetic order, and crystal electric field studies in the Yb^{3+} -based triangular lattice antiferromagnet $\text{Rb}_3\text{Yb}(\text{VO}_4)_2$, *Phys. Rev. B* **112**, 104428 (2025).

[51] D. V. Ambika, Q.-P. Ding, S. J. Sebastian, R. Nath, and Y. Furukawa, Static and dynamic magnetic properties of the spin- $\frac{5}{2}$ triangle lattice antiferromagnet $\text{Na}_3\text{Fe}(\text{PO}_4)_2$ studied by ^{31}P NMR, *J. Phys. Condens. Matter.* **35**, 015803 (2022).

[52] Y. Yamada and A. Sakata, An Analysis Method of Antiferromagnetic Powder Patterns in Spin-Echo NMR under External Fields, *J. Phys. Soc. Jpn.* **55**, 1751 (1986).

[53] K. M. Ranjith, R. Nath, M. Majumder, D. Kasinathan, M. Skoulatos, L. Keller, Y. Skourski, M. Baenitz, and A. A. Tsirlin, Commensurate and incommensurate magnetic order in spin-1 chains stacked on the triangular lattice in $\text{Li}_2\text{NiW}_2\text{O}_8$, *Phys. Rev. B* **94**, 014415 (2016).

[54] K. M. Ranjith, M. Majumder, M. Baenitz, A. A. Tsirlin, and R. Nath, Frustrated three-dimensional antiferromagnet $\text{Li}_2\text{CuW}_2\text{O}_8$: ^{7}Li NMR and the effect of nonmagnetic dilution, *Phys. Rev. B* **92**, 024422 (2015).

[55] R. Nath, Y. Furukawa, F. Borsa, E. E. Kaul, M. Baenitz, C. Geibel, and D. C. Johnston, Single-crystal ^{31}P NMR studies of the frustrated square-lattice compound $\text{Pb}_2(\text{VO})(\text{PO}_4)_2$, *Phys. Rev. B* **80**, 214430 (2009).

[56] M. F. Collins, *Magnetic Critical Scattering* (Oxford University Press, 1989).

[57] Y. Ozeki and N. Ito, Nonequilibrium relaxation method, *J. Phys. A: Math. Theor.* **40**, R149 (2007).

[58] S. T. Bramwell and P. C. W. Holdsworth, Magnetization: A characteristic of the kosterlitz-thouless-berezinskii transition, *Phys. Rev. B* **49**, 8811 (1994).

[59] H. Benner and J. Boucher, *Spin Dynamics in the Paramagnetic Regime: NMR and EPR in Two-Dimensional*

Magnets in Magnetic Properties of Layered Transition Metal Compounds (Editor LJ de Jongh, Kluwer Academic Publishers, Dordrecht, Boston, London, 1990).

[60] J. Cui, Q.-P. Ding, W. R. Meier, A. E. Böhmer, T. Kong, V. Borisov, Y. Lee, S. L. Bud'ko, R. Valentí, P. C. Canfield, and Y. Furukawa, Magnetic fluctuations and superconducting properties of $\text{CaKFe}_4\text{As}_4$ studied by ^{75}As NMR, *Phys. Rev. B* **96**, 104512 (2017).

[61] Q.-P. Ding, W. R. Meier, A. E. Böhmer, S. L. Bud'ko, P. C. Canfield, and Y. Furukawa, NMR study of the new magnetic superconductor $\text{CaK}(\text{Fe}_{0.951}\text{Ni}_{0.049})_4\text{As}_4$: Microscopic coexistence of the hedgehog spin-vortex crystal and superconductivity, *Phys. Rev. B* **96**, 220510 (2017).

[62] Q.-P. Ding, W. R. Meier, J. Cui, M. Xu, A. E. Böhmer, S. L. Bud'ko, P. C. Canfield, and Y. Furukawa, Hedgehog Spin-Vortex Crystal Antiferromagnetic Quantum Criticality in $\text{CaK}(\text{Fe}_{1-x}\text{Ni}_x)_4\text{As}_4$ Revealed by NMR, *Phys. Rev. Lett.* **121**, 137204 (2018).

[63] T. Moriya, The Effect of Electron-Electron Interaction on the Nuclear Spin Relaxation in Metals, *J. Phys. Soc. Jpn.* **18**, 516 (1963).

[64] V. O. Garlea, L. D. Sanjeeva, M. A. McGuire, C. D. Batista, A. M. Samarakoon, D. Graf, B. Winn, F. Ye, C. Hoffmann, and J. W. Kolis, Exotic Magnetic Field-Induced Spin-Superstructures in a Mixed Honeycomb-Triangular Lattice System, *Phys. Rev. X* **9**, 011038 (2019).

[65] A. V. Chubukov and D. I. Golosov, Quantum theory of an antiferromagnet on a triangular lattice in a magnetic field, *J. Phys. Condens. Matter.* **3**, 69 (1991).

[66] Y. Shirata, H. Tanaka, A. Matsuo, and K. Kindo, Experimental Realization of a Spin-1/2 Triangular-Lattice Heisenberg Antiferromagnet, *Phys. Rev. Lett.* **108**, 057205 (2012).

[67] Y. A. Sakhraev, O. Prokhnenco, A. Y. Shapiro, H. D. Zhou, L. E. Svistov, A. P. Reyes, and O. A. Petrenko, High-field magnetic structure of the triangular antiferromagnet $\text{RbFe}(\text{MoO}_4)_2$, *Phys. Rev. B* **105**, 014431 (2022)